Task-Based Trajectories in Iteratively Reconstructed Interventional Cone-Beam CT

J. Webster Stayman and Jeffrey H. Siewerdsen

***Abstract*—Interventional imaging scenarios are rich in prior knowledge of patient anatomy (e.g., preoperative CT and/or successive CBCT scans) and tend to have a specific and well-defined imaging tasks. This presents an opportunity to integrate such information into the image acquisition process by means of a customized CBCT scan orbit in which the source-detector trajectory is chosen based on a knowledge of the task and anatomical context in a manner to maximize performance. We adopt task-based performance predictors based on a numerical (non-prewhitening matched filter) observer model and approximations to the local noise and spatial resolution properties of penalized-likelihood reconstruction. These predictions are then used to identify projections that maximize task performance, beginning with the projection view that maximizes detectability, proceeding to the next-best view, and continuing in an (arbitrarily constrained) orbit that can be physically realized on advanced robotic C-arm platforms. We illustrate the approach in simulations considering a robotic C-arm capable of rotational orbits with oblique angulations to compute orbits that are optimal to a specified imaging task. We demonstrate the performance of task-based trajectory versus simple and complex orbits to illustrate the advantages of integrating prior knowledge and the imaging task into customized acquisitions.**

***Index Terms*—CT Reconstruction, Task-Based Detectability, Interventional Imaging, Cone-beam CT, Model-based Reconstruction, Projection View Optimization.**

I. Introduction

Advanced model-based reconstruction has shown a great deal of promise in its ability to improve noise-resolution tradeoffs over traditional approaches [1] and to accommodate low-fidelity data through exposure reductions or sparse projection sampling[2]. While such methods are now being adopted clinically for diagnostic CT, their use in interventional imaging (e.g., intraoperative CBCT) has yet to be fully explored. There are many aspects of interventional imaging that make it distinct from diagnostic imaging, including: 1) Virtually all patients undergoing image-guided interventions have pre-operative imaging studies offering a wealth of patient-specific anatomical prior knowledge; 2) Interventional systems are well-suited to sparse acquisitions and more general source-detector trajectories (e.g., non-circular orbits); and 3) Imaging tasks associated with interventional imaging are well-defined and highly focused for specific procedures (e.g., detection and localization of known targets). Thus, in many respects, interventional imaging is an ideal target for leveraging advanced model-based reconstruction approaches that accommodate arbitrary orbits and sparsity to customize data acquisitions based on prior knowledge of the patient for maximal performance in specific imaging tasks.

This work was supported in part by NIH Grants No. 2R01-CA-112163 and R21-EB-014964.

J. Webster Stayman is with the Department of Biomedical Engineering, Johns Hopkins University, Baltimore, MD 21212 USA (phone: 410-955-1314; fax: 410-955-1115; e-mail: web.stayman@jhu.edu).

Recent attempts to define acquisitions for increased performance with iterative reconstruction include selection of the number of projections based on condition number [3] and methods that choose projections based on edge content [4]. In this paper, we introduce a framework that leverages previously acquired patient-specific anatomical information to predict the task-based performance of a model-based penalized-likelihood reconstruction for given source-detector trajectories. We then use this framework to select the most information-rich projections that maximize task performance predictions and then assemble a customized task- and patient-specific source-detector trajectory subject to physical / geometrical constraints of the source-detector (robotic C-arm) platform.

II. Methods

A. System Models

Both iterative reconstruction and performance predictors require a system model that must be general enough to accommodate particular acquisition geometries and include measurement noise to leverage the advantages of statistical approaches. We adopt the following general vectorized forward model for the mean measurements:

$$\bar{y} = \mathbf{D}\{b\}\exp\left(-\mathbf{A}\mu\right), \qquad (1)$$

where the measurement vector, y, is related to the volume μ through Beer's Law and includes measurement-dependent gains in the diagonal matrix $\mathbf{D}\{b\}$. Each element of the system matrix, $\mathbf{A}$, models the contribution of a specific voxel to a specific projection measurement. This model can accommodate arbitrary geometries like those obtainable with robotic C-arms (see Figure 1). We note that the system matrix for an entire orbit is comprised of smaller matrices for each 2D projection:

$$\mathbf{A}\begin{pmatrix}\{\theta_1,\phi_1\},\cdots,\\ \{\theta_N,\phi_N\}\end{pmatrix} = \begin{bmatrix}\mathbf{A}_{\theta_1,\phi_1}^T & \mathbf{A}_{\theta_2,\phi_2}^T & \cdots & \mathbf{A}_{\theta_N,\phi_N}^T\end{bmatrix}^T. \qquad (2)$$

In the current work, we focus on a system orbit parameterized by two angles, rotation angle (θ) and obliquity angle (ϕ).While the two angle scenario is an interesting subset

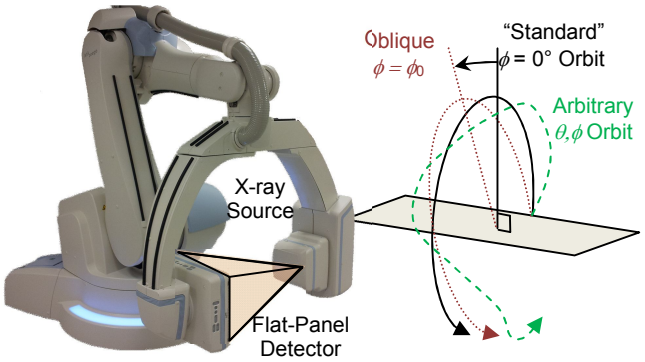

Figure 1: Robotically controlled C-arms are capable of a wide range of source-detector positions. Traditional cone-beam CT acquisitions are typically acquired over a standard 180°+fan angle orbit with no inclination; however, robotic C-arms allow oblique orbits or arbitrarily complex variations in rotation angle (θ) and obliquity (ϕ) throughout the orbit.

of achievable projections, robotic C-arms are capable of translations and modifications of the source-detector distance yielding many more possibilities.

B. Penalized-Likelihood Reconstruction

Once a specific forward model and trajectory has been chosen, it is straightforward to adopt a penalized-likelihood estimation approach for reconstruction. Unlike many analytic approaches, arbitrary trajectories and data sparsity are handled inherently, without modification of weighting factors, etc., once **A** has been defined. We consider the following estimator:

$$\hat{\mu} = \arg\max_{\mu} L(\mu; y) - \beta R(\mu), \tag{3}$$

that adopts a Poisson log-likelihood, L, and a quadratic penalty, $R(\mu)=\mu^T \mathbf{R} \mu$. A separable paraboloidal surrogates approach [5] is applied to iteratively solve (3).

C. Performance Prediction

The estimator in (3) is convenient, since one may write approximate predictors for the local point spread function (PSF) and local covariance [6], or equivalently, the local modulation transfer function (MTF) and local noise-power spectrum (NPS) [7]. Such imaging performance metrics are prevalent in image quality assessment and are leveraged here directly toward the 3D image acquisition and reconstruction process. From [6], the local PSF and covariance are approximately:

$$\begin{aligned} PSF_j &\approx \left[\mathbf{A}^T\mathbf{D}\mathbf{A} + \beta\mathbf{R}\right]^{-1} \mathbf{A}^T\mathbf{D}\mathbf{A} e_j \\ Cov\left\{\hat{\mu}_j\right\} &\approx \left[\mathbf{A}^T\mathbf{D}\mathbf{A} + \beta\mathbf{R}\right]^{-1} \mathbf{A}^T\mathbf{D}\mathbf{A} \left[\mathbf{A}^T\mathbf{D}\mathbf{A} + \beta\mathbf{R}\right]^{-1} e_j \end{aligned} \tag{4}$$

where $\mathbf{D}=\mathbf{D}\{y\}$ and e_j denotes a vector with unity j^{th} element and zero otherwise (specifying the location of interest as with a Kronecker delta function). Note that object-dependence enters (4) through **D,** which is dependent on the measurements. While (4) can be computed precisely using iterative approaches, such methods have high computational burden. Alternately, one may use a Fourier approximation to (4) as in [8]:

$$\begin{aligned} MTF_j &\approx \frac{\mathcal{F}\left\{\mathbf{A}^T\mathbf{D}\mathbf{A}e_j\right\}}{\mathcal{F}\left\{\mathbf{A}^T\mathbf{D}\mathbf{A}e_j + \beta\mathbf{R}e_j\right\}} \\ NPS_j &\approx \frac{\mathcal{F}\left\{\mathbf{A}^T\mathbf{D}\mathbf{A}e_j\right\}}{\left|\mathcal{F}\left\{\mathbf{A}^T\mathbf{D}\mathbf{A}e_j + \beta\mathbf{R}e_j\right\}\right|^2} \end{aligned}, \tag{5}$$

where $\mathcal{F}$ denotes a discrete Fourier transform and the divisions are element-by-element. With expressions for local MTF and NPS, one may predict estimator performance using a model observer. For example, using a non-prewhitening matched-filter observer one can express the detectability index [9, 10] as

$$d'^2 = \frac{\left[\iiint \left(MTF_j \cdot W_{Task}\right)^2 df_x df_y df_z\right]^2}{\iiint NPS_j \cdot \left(MTF_j \cdot W_{Task}\right)^2 df_x df_y df_z}, \tag{6}$$

where W_{Task} is the so-called task function given by the Fourier transform of the difference of two hypotheses (e.g., signal absent vs. signal present). Many other choices of numerical observer are possible, including those that more closely model the human visual system; however, the current initial investigations employ this simple model, which has demonstrated reasonable agreement with human observers in tomographic imaging relative to simple imaging tasks. [10] Thus, using (6), one may then predict performance for a given task (W_{Task}), object (via **D** in (5)), location (subscript j), and acquisition trajectory (**A** in (5)).

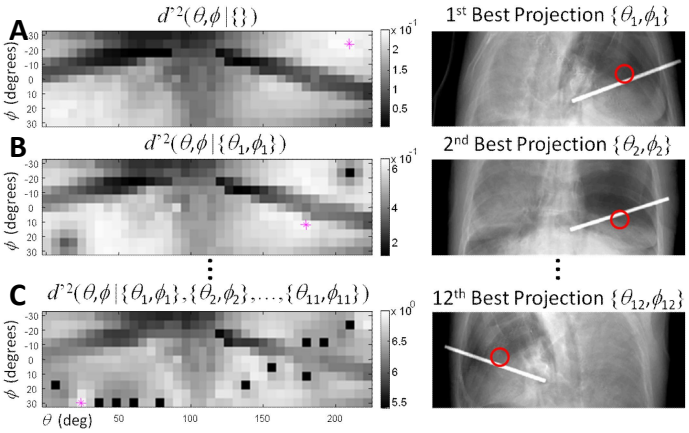

Figure 2: Illustration of the optimization approach used to find angle pairs that contribute to high detectability. The left column shows a detectability map for possible (rotation, obliquity) angle pair additions, the magenta asterisk identifies the new angle pair with highest detectability, and the right column illustrates the projection associated with that particular angle choice. (Since the low-contrast nodule is not visible in the projections, its location is identified with a red circle.) Three passes of the iterative design are shown including: A) Detectability given no previous angles. B) Detectability after addition of the first angle pair. C) Detectability after 11 angle pairs have been added. Note that "best" projections tend to be oblique angles that avoid nodule overlap with the dense surgical tool, and AP/PA projections (with decreased net attenuation) are preferred over lateral projections. Similarly, once an angle is chosen, subsequent detectability maps are decreased in the neighborhood of that angle (and the angle associated with the opposing view – see lower left of 2nd detectability map in (B)).

D. Methodology for Projection Selection

Because we are interested in finding the best source-detector trajectory for a given task and patient in an interventional setting where anatomical information is available from preoperative CT (or prior CBCT), we choose to optimize (6) over **A**. Recalling (2), we may substitute $\mathbf{A}=\mathbf{A}(\{\theta_1,\phi_1\},\ldots,\{\theta_N,\phi_N\})$ for different sets of projections into (6) to obtain $d'^2(\{\theta_1,\phi_1\},\ldots,\{\theta_N,\phi_N\})$.

The general optimization task is difficult, and performing a search over all possible combinations of N angles is prohibitive for larger N. Therefore, we introduce the following notation:

$$d'^2\left(\theta,\phi\middle|\{\theta_1,\phi_1\},\ldots,\{\theta_N,\phi_N\}\right), \tag{7}$$

which denotes a 2D function over θ and ϕ that expresses the overall detectability that a given projection angle yields when added to an orbit already containing a specified set of N projections. In other words, (7) yields a function whose maximum identifies the "next best projection view" based on task detectability. Thus, we may find highly performing sets of projections via a greedy approach where new angles are added to a growing set of projection angles starting with an empty set. That is, a set of projection angles is then constructed by iteratively finding the next most valuable projection $(\theta_{N+1},\phi_{N+1})$ in the detectability map and adding it to the existing set of N angle pairs. Stopping criteria may be formed based on number of angles, dose allocation, acquisition time, detectability, etc.

This greedy optimization approach is illustrated in Figure 2 for a simulated thoracic interventional imaging scenario. In this case, the patient anatomy contains a high-density surgical tool that is part of the intervention as well as a low-contrast pulmonary spherical nodule in a collapsed lung that is difficult to identify in projection images. The task function is the Fourier transform of the spherical nodule, and the location j is

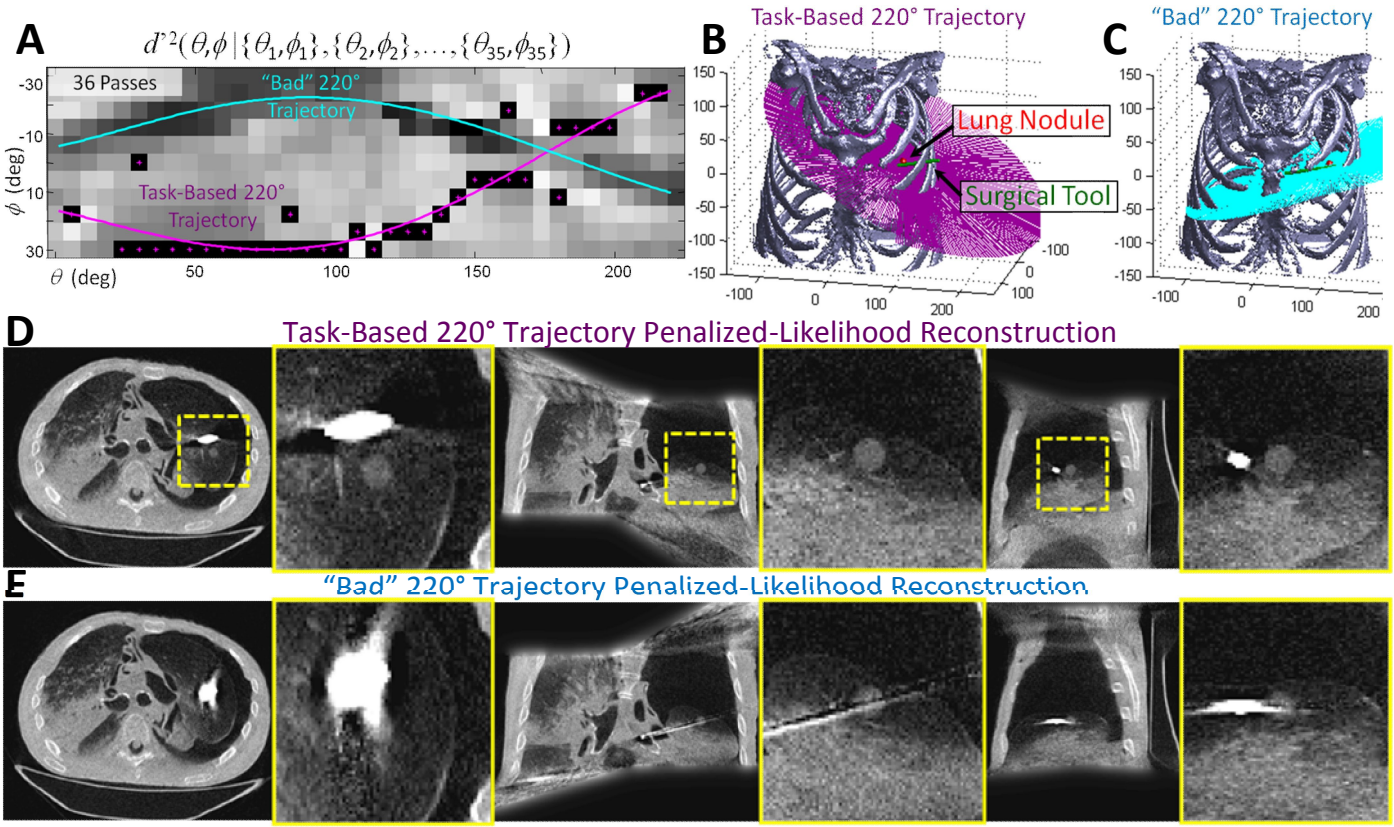

Figure 3: Illustration of a task-based source-detector trajectory using the proposed performance prediction approach. A) The detectability map after 36 passes of optimization. The "best" 36 angular positions are indicated with small magenta asterisks. To obtain a continuous orbit, a polynomial fit was made through these points (magenta curve). Another line fit through the detectability minima represents a particularly "bad" orbit (cyan curve). Representations of the task-based orbit (B) and "bad" orbit scenario (C) are also displayed, showing the source-detector ray that pierces the center of the lung nodule across all projections. Penalized-likelihood reconstruction of acquisitions based on the (D) task-based orbit and (E) "bad" orbit illustrate the relative performance of the two trajectories with all other acquisition and reconstruction parameters held constant. Note that the nodule is more easily detected in the task-based orbit, whereas severe blur around the high-density surgical tool and noise associated with poor data fidelity significantly degrade the image for the "bad" orbit.

matched to the true location of the nodule. Detectability is computed over a limited -30° to 30° obliquity and a 220° rotational range (samples every 6° in each direction); however, these limits may be adjusted to accommodate the mechanical capabilities and constraints for particular devices and interventional scenarios.

III. Results

We continue with the thoracic intervention scenario discussed in the previous section to illustrate the results of the proposed task-based trajectory design approach. In this investigation, a system with 1200 mm source-detector distance, 600 mm source-axis distance, and a 300x800 detector with 0.776 mm pixel pitch was simulated. A 300^3 volume (1 mm voxels) was used for all experiments, and an exposure equivalent of 10^3 photons per detector element was used for Poisson noise generation.

For these studies, we assumed that the image volume is known and perfectly registered for orbital trajectory design. To design a custom orbit for the spherical lung nodule detection task, we conducted 36 passes of the optimization approach detailed in the previous section. The final detectability map and selected angle pairs are shown in Figure 3A. Note that the selected projection angles tend to avoid overlap of the high-density surgical tool and the low-contrast nodule in projections. The influence of the surgical tool is apparent in the upper dark arc in the detectability map. Similarly, while lateral views are discouraged early in the optimization (dark vertical band in Figure 2), these views become important in later iterations (in Figure 3A this dark band is absent).

Interestingly, despite the lack of a constraint for a continuous trajectory, the task-based design has produced largely contiguous projection angle pairs. To produce a completely continuous orbit, we performed a polynomial curve fit through the 36 selected positions to produce a 220° orbit with 1° steps. A second "bad" orbit was also designed via a curve fit through regions of minimum detectability for comparison. These two orbits are illustrated in Figure 3B and C relative to the bony anatomy, lung nodule, and surgical tool. Note that while the task-based orbit avoids projections of the lung nodule that overlap with the surgical tool and bone, the "bad" trajectory is that in which the nodule and tool overlap in nearly every view.

The penalized-likelihood reconstructions associated with each trajectory are shown in Figure 3D and E. The low-contrast pulmonary nodule has qualitatively better detectability in the designed orbit, while the "bad" trajectory results in significantly increased blur and noise due to the low-fidelity data associated with projections through the high-density surgical tool. These effects are most pronounced in the axial images; however, significant streaking and noise is also apparent in the "bad" orbit in the sagittal and coronal slices.

A second experiment using the task-based trajectory design was conducted for a second task function. All simulation settings except for exposure (here set to 10^5 photons per detector element) remain the same as the previous experiment. In this scenario, we selected a task function based on a binary hypothesis test consisting of the same spherical nodule shifted

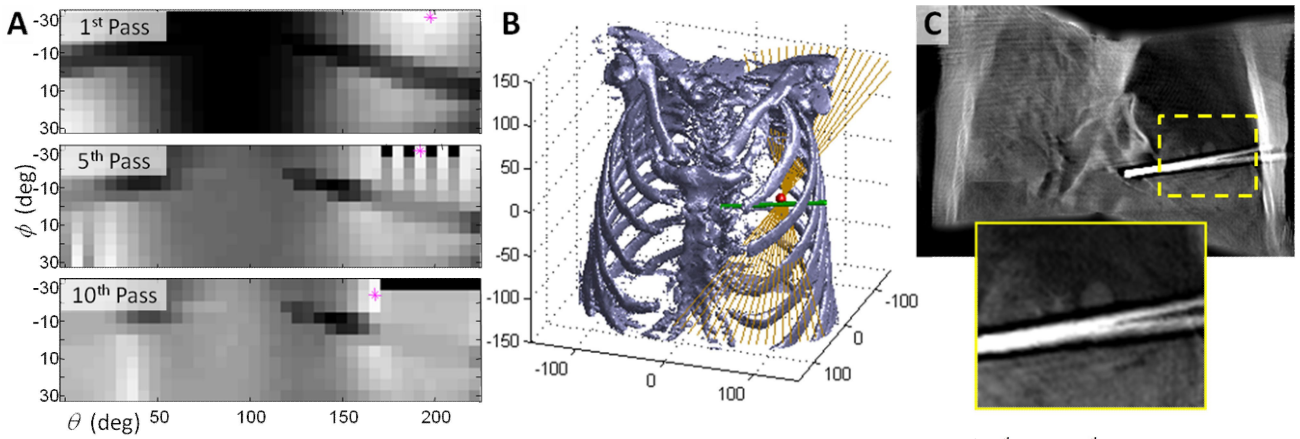

Figure 4: An application of the task-based trajectory design using a lateral localization task function. A) The 1st, 5th, and 10th passes of the optimization procedure show clustering of "next best" angles in the PA/AP direction with a high obliquity that avoids overlap of the nodule and surgical tool. B) A trajectory based on a 3° sampling interval on the best 10 angles is shown. C) Coronal views (appropriate for lateral localization) of a penalized-likelihood reconstruction show strong discrimination of the position of the nodule despite the limited-angle acquisition and small number of projection angles.

1 mm laterally in the patient, emulating a lateral localization task that is very different from the nodule detection task in the first experiment and emphasizing higher spatial frequencies in maximizing the detectability index.

The results of the lateral localization task are summarized in Figure 4. Figure 4A shows the detectability maps for the 1st, 5th, and 10th passes of the trajectory design. The maps reveal a number of interesting features. Not surprisingly, lateral projections contribute little to task performance for the lateral localization task (particularly in early iterations), and AP/PA views with high obliquities that separate the surgical tool and the low-contrast nodule are preferred. In addition, the initial angular pairs are spaced at intervals before filling in later iterations. A trajectory using a 3° sampling interval was fit to the best 10 angle pairs and is illustrated in Figure 4B. The resulting task-based trajectory for lateral localization is a limited angle acquisition (i.e., tomosynthesis). Coronal slices of a penalized-likelihood reconstruction are shown in Figure 4C. Even though the acquisition is highly limited in angle with a small number of views, the nodule is easily localized laterally based on this limited-angle reconstruction.

IV. Discussion

We have introduced a methodology for designing task-based trajectories for interventional imaging using penalized-likelihood reconstruction. The preliminary results show the potential for increased performance over standard orbits, including conventional circular orbits and (unlucky) oblique orbits that align patient anatomy, interventional tools, and/or the structure of interest in a manner that reduces detectability. There are a number of possible extensions to the proposed methodology including generalizations to more arbitrary geometries (e.g., including translation, magnification, etc.), optimization of detectability over a volume-of-interest instead of a single point, optimization of multiple task functions, limited field-of-view reconstructions, and addition of additional constraints (e.g., radiation dose and acquisition time). Another important challenge is an extension of these concepts to nonquadratic penalty approaches that are commonly used in CT.

One important practical consideration for this work is that the methodology presumes having a registered preoperative CT for design. Thus, a functional workflow must include a registration step, perhaps based on an initial projection image and 2D-3D registration. Since this registration is likely imperfect, there is also the possibility of an adaptive design technique that adjusts the orbit "on-the-fly." That is, as more information is obtained about the patient volume, the imaging system adapts its trajectory to maximize performance. The underlying framework presented in this paper is general and can accommodate much of the future work discussed above.

The proposed method leverages the wealth of information available in interventional imaging and combines it with methods of task-based performance evaluation to define optimal trajectories. Whereas traditional approaches tend to neglect the wealth of prior knowledge or use it in only a very coarse manner, the proposed framework integrates it fundamentally into the acquisition process. This is an important step in making imaging systems more aware of the objects they are imaging and the imaging tasks for which they intended, leading to increased imaging performance and potential reduction in dose.

References

[1]J. B. Thibault, *et al.*, "A three-dimensional statistical approach to improved image quality for multislice helical CT," *Med Phys,* vol. 34, pp. 4526-44, Nov 2007.

[2]J. Bian, *et al.*, "Evaluation of sparse-view reconstruction from flat-panel-detector cone-beam CT," *Phys Med Biol,* vol. 55, pp. 6575-99, Nov 21 2010.

[3]E. Y. Sidky, *et al.*, "Sampling conditions for gradient-magnitude sparsity based image reconstruction algorithms," *Medical Imaging 2012: Physics of Medical Imaging,* vol. 8313, 2012.

[4]Z. Zheng and K. Mueller, "Identifying sets of favorable projections for few-view low-dose cone-beam CT scanning," in *11th Int't Meeting on Fully 3D Image Reconstruction in Radiology and Nuclear Medicine*, Potsdam, Germany, 2011, pp. 314-317.

[5]H. Erdogan and J. A. Fessler, "Ordered subsets algorithms for transmission tomography," *Phys Med Biol,* vol. 44, pp. 2835-51, Nov 1999.

[6]J. A. Fessler and W. L. Rogers, "Spatial resolution properties of penalized-likelihood image reconstruction: space-invariant tomographs," *IEEE Trans Image Process,* vol. 5, pp. 1346-58, 1996.

[7]G. Gang, *et al.*, "Modeling and control of nonstationary noise characteristics in filtered-backprojection and penalized-likelihood image recostruction," in *SPIE Medical Imaging*, Orlando, 2013.

[8]J. W. Stayman and J. A. Fessler, "Efficient calculation of resolution and covariance for penalized-likelihood reconstruction in fully 3-D SPECT," *IEEE Trans Med Imaging,* vol. 23, pp. 1543-56, Dec 2004.

[9]R. F. Wagner, *et al.*, "Application of information theory to the assessment of computed tomography," *Medical Physics,* vol. 6, pp. 83-94, 1979.

[10] G. J. Gang, *et al.*, "Analysis of Fourier-domain task-based detectability index in tomosynthesis and cone-beam CT in relation to human observer performance," *Med Phys,* vol. 38, pp. 1754-68, Apr 2011.